

Real-Time Neural BRDF with Spherically Distributed Primitives

YISHUN DOU*, Huawei, China
 ZHONG ZHENG*, Huawei, China
 QIAOQIAO JIN, Shanghai Jiao Tong University, China
 BINGBING NI†, Shanghai Jiao Tong University, China
 YUGANG CHEN, Huawei, China
 JUNXIANG KE, Huawei, China



Fig. 1. Our neural based reflectance model achieves real-time framerate in current high-end desktop machine (i9 12900k and RTX 3090) and can cover a wide range of appearances. We show the time breakdown of evaluating this reflectance model in a *5-maxdepth* path tracer at full resolution (1 SPP, 1920×1080).

We propose a novel compact and efficient neural BRDF offering highly versatile material representation, yet with very-light memory and neural computation consumption towards achieving real-time rendering. The results in Figure 1, rendered at full HD resolution on a current desktop machine, show that our system achieves real-time rendering with a wide variety of appearances, which is approached by the following two designs. On the one hand, noting that bidirectional reflectance is distributed in a very sparse high-dimensional subspace, we propose to project the BRDF into two low-dimensional components, *i.e.*, two hemisphere feature-grids for incoming and outgoing directions, respectively. On the other hand, learnable neural

reflectance primitives are distributed on our highly-tailored spherical surface grid, which offer informative features for each component and alleviate the conventional heavy feature learning network to a much smaller one, leading to very fast evaluation. These primitives are centrally stored in a codebook and can be shared across multiple grids and even across materials, based on the low-cost indices stored in material-specific spherical surface grids. Our neural BRDF, which is agnostic to the material, provides a unified framework that can represent a variety of materials in consistent manner. Comprehensive experimental results on measured BRDF compression, Monte Carlo simulated BRDF acceleration, and extension to spatially varying effect demonstrate the superior quality and generalizability achieved by the proposed scheme.

*Both authors contributed equally to this research
 †Corresponding Author: Bingbing Ni

Authors' addresses: Yishun Dou, Huawei, China, yishun.dou@gmail.com; Zhong Zheng, Huawei, China, zhengzhong5@huawei.com; Qiaoqiao Jin, Shanghai Jiao Tong University, China, zhengzhong5@huawei.com; Bingbing Ni, Shanghai Jiao Tong University, China, nibingbing@sjtu.com; Yugang Chen, Huawei, China; Junxiang Ke, Huawei, China.

CCS Concepts: • **Computing methodologies** → **Reflectance modeling; Rendering.**

Additional Key Words and Phrases: Real-Time, Material, Rendering, BRDF, Neural Network

1 INTRODUCTION

Reflectance model is one of the most critical factors that affects the rendering photorealism. A common choice for *real-time* rendering is hand-crafted analytical BRDF models [Burley and Studios 2012; Walter et al. 2007], while they often struggle with reproducing realistic appearance. As for the methods offering high realism, measured BRDF models incur prohibitive storage and transmission overhead, especially for anisotropic and spatially varying materials; Monte Carlo simulation models rely on a large number of light paths, which prevents their popularity in real-time applications.

One attractive choice is approximating the reflectance by implicit neural network [Park et al. 2019], which has compact storage and can be potentially accelerated by the recent emerged feature-grid encoding [Müller et al. 2022; Takikawa et al. 2022]. However, the 6D input to the BRDF poses challenges for building such an acceleration structure. We propose to alleviate this difficulty through a *factorization* which decomposes the BRDF to two 3D hemisphere feature-grids that are then decoded by a tiny MLP. Our system is designed according to the following principles:

- **Efficiency.** BRDF evaluation at shading point would executes million times on full HD resolution. Operations on spherical feature-grid should be simple and the neural network should be kept lightweight.
- **Mild memory cost.** The feature-grid is instance-specific and often trades memory for fast evaluation. Hence, we should maximize the memory-quality tradeoff.
- **Generalization.** We aim at providing a unified framework for a wide range of materials. We strive for a solution that is agnostic to the materials of isotropic or anisotropic, measured or simulated, spatially varying or not, and dense sampling or sparse.

The first principle spurs us to construct informative feature-grid that alleviates the heavy feature learning network to a much smaller one. It is also confronted with challenges in sphere pixelation. To this end, we exhaust commonly used sphere discretization methods, which are discussed and experimented in this paper. Moreover, the chosen HEALPix [Gorski et al. 2005] sphere pixelation is then tailored for constructing our reflectance feature-grid.

The second principle poses challenges for the methods that directly store separate features at each grid [Müller et al. 2022; Takikawa et al. 2021]. To maximize the memory utilization, we propose to use neural reflectance primitives. These primitives are centrally stored in a codebook and can be shared across multiple grids and even across materials. As a result, the sphere grid is only required to store the low-cost index pointing to primitive and a material could be approximated by decoding a combination of these primitive codes, *i.e.* a good tradeoff between representation capability and memory compactness.

Built on an auto-decoder framework, the factorization is implicitly achieved during the end-to-end joint training. Our **Neural BRDF** (NeuBRDF) enjoys the following properties:

- NeuBRDF represents measured or offline simulated materials effectively and can be evaluated in *real-time* at rendering.
- NeuBRDF provides a *unified framework* for a rich diversity of materials in a consistent manner.

- Memory-quality tradeoffs can be easily achieved.
- With a neural texture, NeuBRDF can be used for SVBRDF.

2 BACKGROUND AND RELATED WORK

Our approach is related to many previous works in BRDF factorization, feature-based neural representations, neural reflectance models, and sphere pixelation. We explore the connection among the areas below.

BRDF Factorization. Suitable analytic models are not always available for a desired effect, and directly tabulating reflectance data is prohibitive due to the high dimensionality. To overcome this limitation, some pioneers have proposed to factorize the BRDF function into lower dimensional factors, such as spherical harmonics [Westin et al. 1992], Zernike polynomials [Koenderink et al. 1996] and so on. Factors are weighted summed or producted [Latta and Kolb 2002; McCool et al. 2001] to approximate the high dimensional BRDF function. Similarly, Bagher et al. [2016] define a non-parametric factor microfacet model using tabulated definitions for three functional components (D , G , and F). A commonality among these methods is they fall in linear transformation (or with one non-linearity). In contrast, our factorization achieved via auto-decoder learning is capable of modeling complex non-linear functions. In other words, the relationship between existing factorization and ours is similar to that of PCA and auto-encoder.

Feature-based Neural Representation. Feature-based approaches use differentiable feature primitives to represent the scene including geometric shapes and materials. In terms of geometric shapes, feature-based approaches discretize the spatial space into a multi-scale regular grid and store local features in an octree-based volume [Takikawa et al. 2021], a hash table [Müller et al. 2022], or a dictionary [Takikawa et al. 2022]. Focusing on materials is much harder than geometric shapes since typically used BRDFs have a higher input dimension (6D) than the 3D geometry. However, expanding the 3D spatial grid directly into higher dimensions to capture BRDFs is prohibitive for its large memory footprint.

Neural Reflectance Models. There are two kinds of approaches for neural based SVBRDF / BTF / BRDF modeling. One kind of approaches use one neural network to represent one material. For example, [Sztrajman et al. 2021] used different lightweight networks to represent BRDFs of different materials, and the autoencoder architecture achieves compact representation. In order to represent and render a variety of material appearances at different scales, NeuMIP was proposed by [Kuznetsov 2021]. [Rainer et al. 2019] used a latent vector to represent each texel as a neural representation of BTFs. Most recently, [Fan et al. 2023] approximated a BTF with a function of 2D spatial coordinates and half-vector coordinates. However, the half-vector poses a great risk of loss of bidirectional reflectance and thus requires a heavy MLP decoder for correction. The other kind of approaches use one neural network to represent a variety of materials. [Rainer et al. 2020] represented all materials with a unified model, which also uses the autoencoder architecture. But this approach may lead to a decline in the quality of representation. In order to realize the compact representation and keep the high

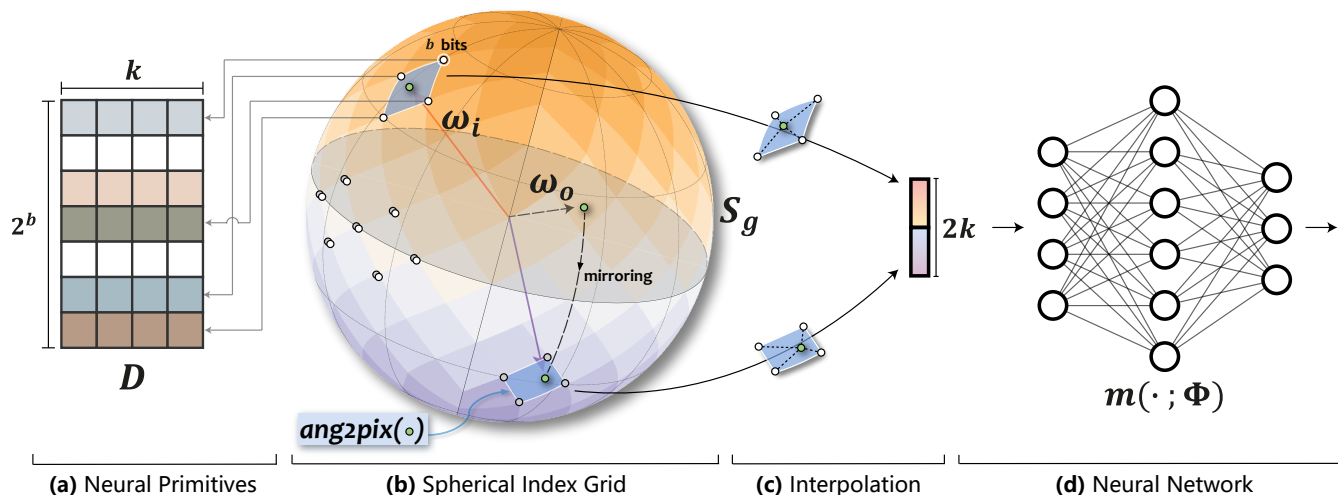


Fig. 2. **Illustration of the neural BRDF with spherically distributed primitives.** (a) Learnable neural reflectance primitives are centrally stored on a codebook \mathcal{D} . (b) Given the incident direction ω_i and outgoing ω_o , we find the surrounding pixels independently on a spherical index grid S_g . For all resulting corner indices, we look up the corresponding k -dimensional neural primitive from the codebook. (c) Interpolating them according to the relative position of ω_i and ω_o within the respective curvilinear quadrilateral pixels. (d) A tiny MLP takes the concatenated features and outputs final bidirectional reflectance value.

quality of recovery, deepBRDF was proposed by [Hu et al. 2020], which uses a convolutional neural network. The neural process also was proposed by [Zheng et al. 2021] for a compact representation of measured BRDFs. Recently, [Fan et al. 2022] proposed to perform layering in the neural space with the latent code compressed by a neural network.

Sphere Pixelation. Feature-grid relies on a well-characterised spatial pixelation, such as the octree for the neural SDF representation [Takikawa et al. 2021]. Besides, representing materials spurs a demand of exploiting a sphere pixelation to accommodate spherical distributed features. We employ the Hierarchical Equal Area isoLatitude Pixelation (HEALPix) [Gorski et al. 2005], which was designed for efficient and incremental discretization of full-sky maps in application to the satellite missions to measure the cosmic microwave background in astrophysics [Perraudin et al. 2019]. It provides a deterministic, uniform, and hierarchical sampling method for the sphere surface. Other sphere pixelation methods, such as longitude-latitude lattice, Layered Sukharev grid [Sukharev 1971], and Fibonacci lattice [González 2010], are inadequate in term of efficiency or effectiveness, which will be discussed and experimented in this article.

3 METHOD

Our goal is to represent bidirectional reflectance distribution function (BRDF) using a neural framework that maps bidirections to reflectance values and is evaluated in *real-time* with *mild memory cost*. The material is one of the most critical factors that affects the rendering photorealism, yet existing realistic approaches either incur large memory overhead or are computationally expensive. We therefore opt for approximating it to keep the cost down.

The key idea is to build a neural framework that consists of a low-dimensional tailored feature-grid and a tiny neural network to

approximate the high-dimensional bidirectional reflectance distributions. In this section, we discuss the algorithmic choices that are key to satisfy the design principles outlined in Section 1. Implementation and practice consideration are discussed in Section 4.

3.1 Algorithm Overview

Evaluating the NeuBRDF consists of **querying** a spherical index grid S_g by directions ω_i and ω_o , **lookup** the codebook \mathcal{D} , and **inference** a tiny MLP; see Figure 2 for an illustration.

Fast Evaluation. To enable effective and efficient BRDF evaluation at rendering, we leverage the implicit field which bases on *feature-grid*. In contrast to the *global* methods (e.g. NeRF [Mildenhall et al. 2021]) that consist entirely of an MLP, the feature-grid allows the use of a much smaller network. However, it is prohibitive to expand the commonly used 3D spatial grid (e.g. NGP [Müller et al. 2022]) in scene representation directly into higher dimensions to capture BRDFs, since a 3D one already incurs a large memory footprint.

We consider that the bidirectional reflectance is distributed in a very sparse high-dimensional subspace and therefore propose to factorize the BRDF as a combination of low-dimensional components. Concretely, we project the 6D BRDF onto two compact 3D hemispherical surface feature-grids along the outgoing ω_o and incident ω_i directions. These two factors are used to compute the final reflectance via a tiny neural network, leading to efficient evaluation.

Memory Policy. A tradeoff with feature-grid representations is that they can be quickly evaluated, but typically have a large memory overhead to cache the bulky features. While our factorization-based solution offers dimensionality reduction, caching the 3D hemispherical features still incurs significant overhead. Furthermore, the learned feature-grid is instance-specific, which means that the memory cost grows with the number of materials in the rendering scenes.

To this end, we incorporate the vector quantization (VQ) compression technique. The features that full of the hemisphere surface grid are replaced with indices into a learned codebook [Takikawa et al. 2022]. Notably, we could further maximize the memory-quality tradeoff by reusing one codebook for an arbitrary number of materials, where each material has an exclusive indices grid. We therefore term the prototype vectors in the codebook the *neural reflectance primitives*. These primitives, the indices, and the tiny MLP network are all trained jointly.

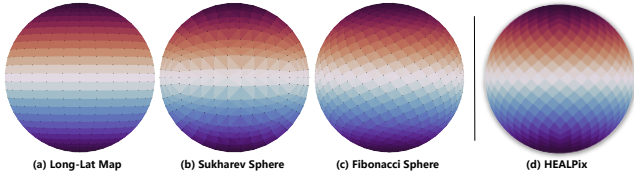


Fig. 3. Comparison among different sphere pixelations.

3.2 Spherical Feature-Grid

Neural implicit fields in previous works are mainly used to represent low-dimensional signals, such as images and SDFs, thus typically a 3D grid is sufficient for the variants that base on feature-grid. Even for the application of representing 5D radiance fields, the feature-grids are still built in 3D space, which represent the radiance by spherical harmonics [Fridovich-Keil et al. 2022] or only represent the Lambertian effect [Müller et al. 2022]. In our case, the 6D BRDF is projected along the outgoing ω_o and incident ω_i directions, resulting in two factors that are used to compute reflectance value.

Each factor is represented by features distributed on a hemisphere surface \mathcal{H} , where the features are located in some discretized grid. Although there are several spherical discretization methods, whether they meet the needs of real-time BRDF remains to be discussed. Here we explore a structure that is appropriate for BRDF.

3.2.1 Principles and Choices. Discretizing the sphere surface is much more complicated than that of the cube volume used in scene representation, in terms of uniform pixelation and fast pixel indexing, both of which are naturally achieved by the cube volume with regular discretization but pose challenges for the sphere surface. To achieve the post pruning for sparse measurements, the property of hierarchy is required. That is, unsupervised pixels should be replaced with their parent (macro) pixel, resulting in a multi-resolution sparse grid at runtime. Together, the sphere discretization should meet the following main requirements:

- **Uniform Pixelation.** Firstly, it conforms to the pixelation principle of image or voxel. Secondly, the sphere pixelation should be agnostic of materials and sampling strategies.
- **Fast Indexing.** Real-time rendering requires fast indexing of sphere pixels in arbitrary direction.
- **Hierarchy.** For sparse measurements, a post grid pruning is necessary. The intrinsic hierarchy is required to supported multi-resolution sparse grids.

There exist several sphere discretization choices, such as longitude-latitude lattice, Layered Sukharev grid [Sukharev 1971], Fibonacci

Table 1. Comparison of pixelation methods. **Indexing:** time consumption of obtaining the corresponding pixel p given bidirection ω_i and ω_o for a 1920×1080 frame. **Iso-Latitude:** an essential factor for consistent modeling of the Fresnel term of reflectance at various azimuth angles.

Pixelation	Uniform	Indexing	Hierarchy	Iso-Lat
Long-Lat	No	< 0.5ms	No	Yes
Sukharev	No	~ 5ms	No	No
Fibonacci	Yes	~ 5ms	No	No
HEALPix	Yes	< 0.5ms	Yes	Yes

lattice [González 2010], and Hierarchical Equal Area isoLatitude Pixelation (HEALPix) [Gorski et al. 2005]. Figure 3 illustrates the comparison of these choices. The simplest longitude-latitude lattice is suitable for indexing which is directly achieved by rounding up and down, but it arranges too many grid points on the polar cap. Sukharev grid also fails to achieve uniform pixelation. Although Fibonacci lattice can evenly distribute points on a sphere surface, it cannot locate the pixel for a given direction analytically and requires a nearest neighbor search, which prevents it from being used in real-time rendering. In contrast, HEALPix satisfies the above requirements; summarized in Table 1. We therefore employ HEALPix as the underlying sphere grid of our neural BRDF framework. Moreover, the intrinsic hierarchy of HEALPix facilitates grid pruning for isotropic reflectance or sparse measurements, which we will discuss in Section 4.

3.2.2 HEALPix-Based Data Structure. HEALPix tessellates the sphere into equal area curvilinear quadrilaterals. The base resolution comprises 12 pixels in three rings around the poles and equator. The resolution of the grid is determined only by one hyperparameter N_{side} , which defines the number of divisions along the side of a base-resolution pixel. As a result, a HEALPix map has $12N_{side}^2$ pixels and $12N_{side}^2 + 2$ grid points, where the pixels have the same area.

Unlike prior work that used HEALPix for cosmological applications [Perraudin et al. 2019], we arrange features to points at grid corner instead of the pixel center; Figure 4 shows the comparison. This design reduces the computation cost of pixel indexing for four nearest neighboring features. Although arranging features at the grid center has a modest indexing cost for nine nearest neighbors, the number of memory accesses doubles due to the excessive number of features.

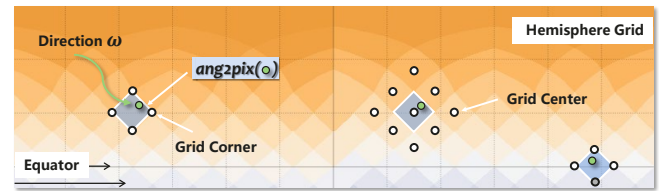


Fig. 4. Illustration of our hemisphere grid in Cartesian coordinate. Arranging features at grid corner ease the query of nearest neighboring features. A hemisphere in our design includes pixels covering the equator.

Consider a hemisphere covering equator line (*i.e.* a ring adjacent to the equator line in another hemisphere is included). The number

of the hemisphere grid points is $n = 6N_{side}^2 + 6N_{side} + 1$ ¹. We denote a hemispherical feature-grid as $\mathcal{H}_g \in \mathbb{R}^{n \times k}$, where k is the feature dimension.

Given a query direction $\omega = (\theta, \phi)$, where $\theta \in [0, \pi]$ is the colatitude in radians measured from the north pole and ϕ is the longitude in radians measured eastward. **(a)** We first find the curvilinear quadrilateral p to which the direction ω belongs, through the fast analytic indexing *ang2pix*. We refer the readers to the reference [Gorski et al. 2005] for details. **(b)** Then we extract the features $z_p^t \in \mathcal{H}_g$ at four corners of the quadrilateral pixel p , where $t \in \{1, 2, 3, 4\}$ is the local indices. Meanwhile, we fetch the corresponding spherical coordinates ω_p^t to compute the interpolation weights w_p^t during training, where the weights are assigned with $1/4$ at runtime for efficiency:

$$w_p^t = \begin{cases} w_p^t / \sum_{j=1}^4 w_p^j, & \text{where } w_p^t = 1/d_p^t, \quad \text{Training,} \\ 1/4, & \text{Runtime,} \end{cases} \quad (1)$$

where d_p^t is the great-circle distance between the spherical coordinates of ω_p^t and ω . The query for a hemispherical feature-grid \mathcal{H}_g by ω can be expressed as:

$$\psi(\omega; \mathcal{H}_g) = \sum_{t=1}^4 w_p^t z_p^t, \quad \text{where } p = \text{ang2pix}(\omega; \mathcal{H}_g), \quad (2)$$

(c) Recall that this process takes place independently for incident ω_i and outgoing ω_o and therefore two hemispherical feature-grids are required for representing these two factors. Effectively, we merge the two hemispheres into a sphere that comprises three duplicate rings, the equator and its two nearest adjacent rings. The number of the sphere grid points $2n$, i.e. $12N_{side}^2 + 12N_{side} + 2$. We denote a spherical feature-grid as $\mathcal{S}_g \in \mathbb{R}^{2n \times k}$. Eventually, querying a spherical grid \mathcal{S}_g by ω_i and ω_o is:

$$\begin{aligned} \hat{\omega}_o &= (\pi - \omega_o, \theta, \omega_o, \phi), \\ \psi(\omega_i, \omega_o; \mathcal{S}_g) &= [\psi(\omega_i; \mathcal{S}_g^+), \psi(\hat{\omega}_o; \mathcal{S}_g^-)], \end{aligned} \quad (3)$$

where $[\cdot, \cdot]$ denotes concatenation. The \mathcal{S}_g^+ and \mathcal{S}_g^- denote the north and south hemispherical feature-grid, both of which include the equator ring and a nearest adjacent ring to the equator in another hemisphere.

3.2.3 Decoder. In order to lift the partially low-dimensional factors to the original 6D space, we employ a multilayer perceptron (MLP) as a non-linear decoder, where the input to MLP is the result of spherical feature-grid query $\psi(\omega_i, \omega_o; \mathcal{S}_g)$. Then, the BRDF $f(\omega_i, \omega_o)$ of our method is described as:

$$f(\omega_i, \omega_o) \approx m(\psi(\omega_i, \omega_o; \mathcal{S}_g); \Phi), \quad (4)$$

where $m(\cdot; \Phi)$ is the MLP with parameters Φ (including weights and biases). Interestingly, the architecture designed from the perspective of factorizing the 6D BRDF resembles that from the parametric encoding [Liu et al. 2020; Müller et al. 2022; Peng et al. 2020; Takikawa et al. 2021]. The additional trainable parameters (beyond weights and biases) allow the use of a tiny MLP without sacrificing representation quality and yield immediate *benefits*: (1) NeuBRDF can be

¹A ring in equatorial belt comprises $4N_{side}$ points [Gorski et al. 2005]. The hemisphere excluding equator has $6N_{side}^2 - 2N_{side} + 1$ points.

trained to convergence much faster than the method that consists entirely of MLPs; (2) It provides feasibility for applying neural BRDF to real-time rendering applications.

Discussion. The difference between parametric-encoding methods and ours is obvious in the intention of MLP. Conceptually, the MLP in our framework is used to *compensate* the lossy factorization. Whereas for methods with parametric encoding, the MLPs are typically used for local (interpolated) feature decoding [Peng et al. 2020], multi-resolution aggregation [Takikawa et al. 2021], or handling non-Lambertian effect [Müller et al. 2022] for neural radiance application.

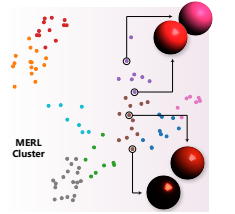
3.3 Neural Reflectance Primitives

While our factorization solution can perform dimensionality reduction, a spherical feature-grid \mathcal{S}_g with our default setting still requires about 0.8 million parameters ($N_{side} = 64, k = 16$). Following [Takikawa et al. 2022], we compress the storage by incorporating vector-quantization into our framework. Concretely, the $\mathcal{S}_g \in \mathbb{R}^{2n \times k}$ is compressed into an integer vector $\mathcal{S}_g \in \mathbb{Z}^{2n}$ with the range $[0, 2^b - 1]$. The integers are used as *indices* into a codebook matrix $\mathcal{D} \in \mathbb{R}^{2^b \times k}$, where b is the bitwidth to store such an integer. We thus now name \mathcal{S}_g the spherical index grid. The BRDF $f(\omega_i, \omega_o)$ is computed as:

$$f(\omega_i, \omega_o) \approx m(\psi(\omega_i, \omega_o; \mathcal{D}[\mathcal{S}_g]); \Phi), \quad (5)$$

where $[\cdot]$ is the indexing operation and $\mathcal{D}[\mathcal{S}_g]$ denotes lookup. (The training of these indices is detailed in Section 4.) For *fp16* storage, this gives us a compression ratio of $16 \cdot 2n \cdot k / (2n \cdot b + 16 \cdot k \cdot 2^b)$, which can be orders of magnitude when b is small and n is large.

Notably, we provide an option to *maximize* the quality-cost trade-off for deploying NeuBRDF into memory constrained devices. Consider that both the aforementioned codebook and spherical index grid are material-specific. Here, we aim at developing a set of *neural reflectance primitives* that are learned and shared across multiple materials that have similar characteristics. Specifically, we first use a convolutional auto-encoder with bottleneck architecture, of which the objective is to reconstruct the raw reflectance data. The information bottleneck prompts clusters of similar materials. Thus, a clustering algorithm such as K-Means is then applied to the learned bottleneck codes. For a cluster with m materials, we instantiate an MLP, a codebook storing the primitives, and m spherical index grids \mathcal{S}_g , i.e. only the low-cost integer indices are exclusive. Still, both of these modules are trained jointly.



4 IMPLEMENTATION

This section describes the implementation details in terms of efficient training, performance at runtime, and extension applications.

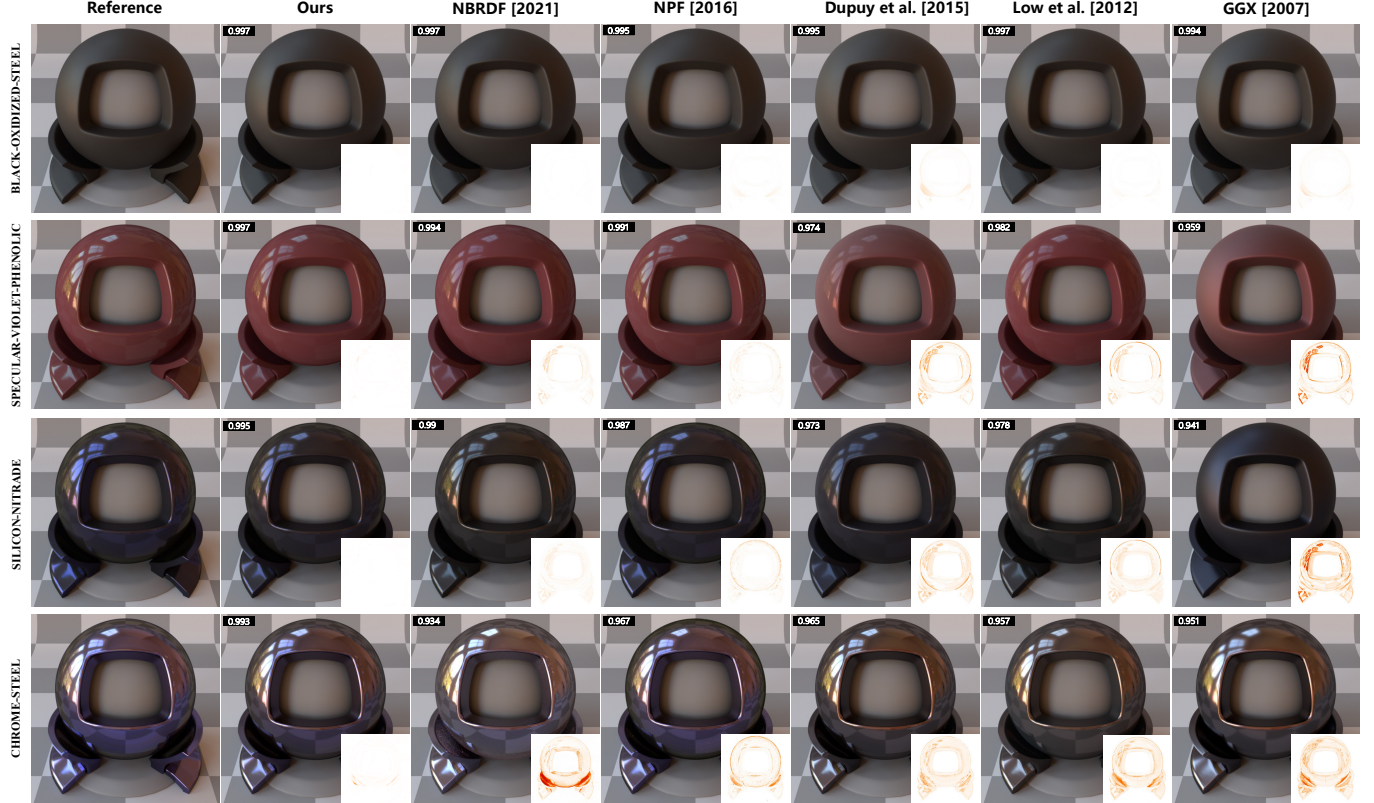


Fig. 5. **Quality comparison in fitting reflectance models to MERL [2003] measurements.** The analytical microfacet reflectance models, including GGX and Low et al, struggle in representing the highly frequency changes (SILICON-NITRIDE) and often lead to color shift (CHROME-STEEL). Compared with the previous factorization-based methods, NPF [2016] and Dupuy et al. [2015], where the NPF demonstrates fair visual effect, our method shows better qualitative results. We show the SSIM value in top-left corner and SSIM pixel-value in bottom-right, following NBRDF [2021] for fair comparison.

Training. Given bidirections ω_i, ω_o and ground truth reflectance values y that are obtained via measurement or simulation, the optimization problem is:

$$\arg \min_{\mathcal{D}, \mathcal{S}_g, \Phi} \mathbb{E}_{\omega_i, \omega_o, y} \|m(\psi(\omega_i, \omega_o; \mathcal{D}[\mathcal{S}_g]); \Phi) - y\|. \quad (6)$$

This cannot be solved directly by usual gradient methods since the indexing $\mathcal{D}[\mathcal{S}_g]$ is non-differentiable. To this end, we use a proxy soften matrix $C \in \mathbb{R}^{2n \times 2^b}$ from which the integer indices $\mathcal{S}_g = \arg \max_j C[j]$ can be obtained from row-wise argmax, following [Takikawa et al. 2022]. We can then replace the hard indexing $\mathcal{D}[\mathcal{S}_g]$ with a matrix product $\sigma(C)\mathcal{D}$, where $\sigma(\cdot)$ is the softmax function applied row-wise on matrix C .

For efficient training and better convergence, we expect the argmax results will almost freeze after a training period and the gradient that is backpropagated from a grid point of \mathcal{S}_g mainly affects single corresponding primitive. That is, we should adjust the softness during training. Accordingly, we introduce a tunable temperature hyperparameter τ to the softmax. We obtain the following optimization problem:

$$\arg \min_{\mathcal{D}, \mathcal{S}_g, \Phi} \mathbb{E}_{\omega_i, \omega_o, y} \|m(\psi(\omega_i, \omega_o; \sigma_\tau(C)\mathcal{D}); \Phi) - y\|, \quad (7)$$

where the temperature softmax is $\sigma_\tau(\mathbf{x}_i) = \exp(\mathbf{x}_i/\tau)/\sum_j \exp(\mathbf{x}_j/\tau)$. The hyperparameter τ controls the softness of the probability distribution. When τ gets lower, the biggest value in \mathbf{x} gets more probability. In our case, τ is initialized with 1.0 and decreased linearly with the training epoch until the minimum 0.5. We also use the straight-through estimator [Bengio et al. 2013] to make the loss be aware of the hard indexing during training, *i.e.* we use Equation 6 for forward pass and Equation 7 for backward pass. We jointly train the codebook entries, the indices, and the MLP by applying Adam [Kingma and Ba 2014], where we initialize learning rate to 10^{-2} that is then decayed using multistep scheduler.

Tiny Neural Network. A lightweight neural network is made possible when the informative features are fed. Our fully connected neural network comprises of four fully connected layers. The two hidden layers have 64 neurons each with ReLU activation functions.

Sphere Grid Pruning. The measured database is typically acquired using a gonireflectometer with motorized robotic arms. The acquisition setups, such as the angular resolution of sensors and lights, vary widely among different databases. Due to the uniform pixelation of our spherical grid, our framework can adapt to data with different sampling strategies. However, there may be some grid

Table 2. Materials used in our experiments. **TYPE**: BRDF, BTF and SVBRDF are included. **SAMPLES**: Sparse measurements are involved to assess the generalization ability of NeuBRDF. **SOURCE**: Both the reflectance measured from real-world, simulated by Monte Carlo methods, and evaluated over analytic models are considered. (* isotropic, ° anisotropic.)

DATABASE	TYPE	SAMPLES	SOURCE
MERL	BRDF*	Dense	Measured
RGL	BRDF*	Dense	Analytic
LayeredBRDF	SVBRDF*	Dense	Simulated
Special Coatings	BRDF*	448/576	Measured
UBO2014	BTF°	22801	Measured
UBOFAB19	SVBRDF°	100	Measured

points that are never supervised during training. For efficiency at runtime and meaningful feature query, we discard these points before deployment. That is, a grid point is removed if there is no training direction ω locating at the surrounding four pixels. Recall that the HEALPix is hierarchical, *i.e.* a pixel is divided into four at next level, we can thus naturally replace these four pixels with their parent, which is similar with pruning an octree in [Takikawa et al. 2021].

This pruning strategy is useful for isotropic materials or sparse measurements. For the isotropic materials, such as those in MERL [Matusik et al. 2003], only about quarter spherical grids are preserved after pruning.¹ For the sparse measurements, our method behaves more like an analytic method, where we can simply infer any given direction, rather than resorting to time-consuming nearest neighbor search and interpolation like rendering directly with measured data. Figure 7 shows a rendering of a NeuBRDF model trained on a sparse measurement (448 sampled bidirections) [Ferrero et al. 2014].

SVBRDF and BTF. Given 2D location coordinates $\mathbf{u} \in \mathbb{R}^2$, incident and outgoing directions, the spatially varying BRDF (SVBRDF) or bidirectional texture function (BTF) [Dana et al. 1999] outputs a reflectance value. We discuss these two together since our method focuses on evaluation rather than direction sampling.

We propose to use the neural texture [Thies et al. 2019] as a *plugin* for our NeuBRDF. Concretely, we define the neural texture $\mathcal{T} \in \mathbb{R}^{h \times w \times c}$ where c is the texture channel. The neural texture lookup $\varphi(\mathbf{u}; \mathcal{T})$ is achieved by grid sampling, where \mathbf{u} is the UV coordinate at the shading point. The resulting texture vector, together with the feature from spherical grid, are fed to the MLP $m(\cdot, \Phi)$, which predicts the SVBRDF / BTF value:

$$f(\omega_i, \omega_o, \mathbf{u}) \approx m([\psi(\omega_i, \omega_o; \mathcal{D}[S_g]), \varphi(\mathbf{u}; \mathcal{T}); \Phi). \quad (8)$$

5 EXPERIMENTS

5.1 Experimental Setups

We implement the training in PyTorch [Paszke et al. 2019]. After pruning the unused the spherical grid, the NeuBRDF is ready for deploying into real-time rendering framework. We then deploy the runtime version in Falcor [Kallweit et al. 2022] for real-time testing (Figure 1) and in Mitsuba [Jakob 2010] for fair comparison

¹For isotropic materials, we assign the $\omega_o \cdot \phi$ to azimuth difference with the range $[0, \pi]$ and leave $\omega_i \cdot \phi = 0$. Therefore, after pruning, about half pixels are kept in south hemisphere and only pixels surrounding 0 longitude line are kept in north hemisphere.

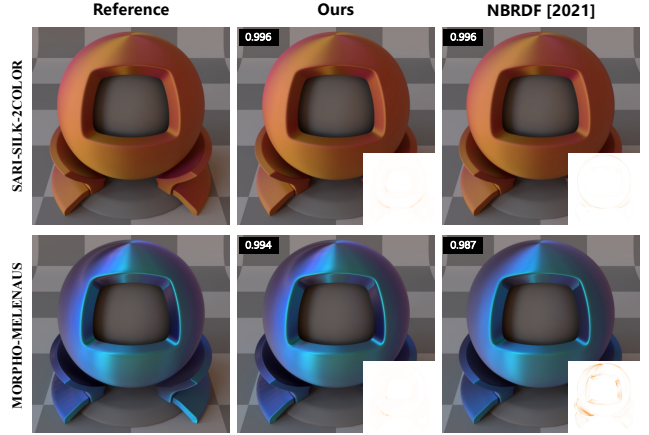


Fig. 6. **Quality comparison in representing anisotropic materials from RGL [2018] database.** Our method well preserves the highly frequent changes on appearance, especially in the complicated MORPHO-MELENAUS. We show the SSIM value in top-left corner and SSIM pixel-value in bottom-right, following NBRDF [2021] for fair comparison.



Fig. 7. **NeuBRDF trained on sparse measurements.** Our approach can generalize to sparse measurements for both the BRDF (bottles) [Ferrero et al. 2014] and SVBRDF (table cloth) [Merzbach et al. 2019]. *Bottles*: With our grid pruning, unsupervised pixels are replaced with their parent, resulting in a smooth rendering. *Table Cloth*: NeuBRDF shows faithful rendering effect compared with the measured counterpart.

with some methods implemented in this framework. We use the following model configuration unless otherwise specified: $N_{side} = 64$, $k = 16$, $b = 9$ and the MLP has 2 hidden layers with 64 neurons.

Datasets. To demonstrate the versatility of NeuBRDF, we extensively experiment on various materials. The databases used in our experiments are listed in Table 2, including isotropic BRDFs, anisotropic BRDFs, and spatially varying BRDFs, where the data sources are chosen deliberately to span measured, analytic, and simulated material. We also select some very sparse measurement (such as the Special Coating [Ferrero et al. 2014]) to demonstrate the generalizability of NeuBRDF and the effectiveness of sphere grid pruning.

Baselines. We compare our method to several strong BRDF baselines: (1) the usual parametrized microfacet model GGX [Walter et al. 2007] and the state-of-the-art one proposed by Low et al. [2012]; (2) the recent non-parametric methods relied on factorization [Bagher et al. 2016; Dupuy et al. 2015]; (3) neural approaches for BRDF [Sztajman et al. 2021], Layered BRDF [Fan et al. 2022], and BTF [Fan

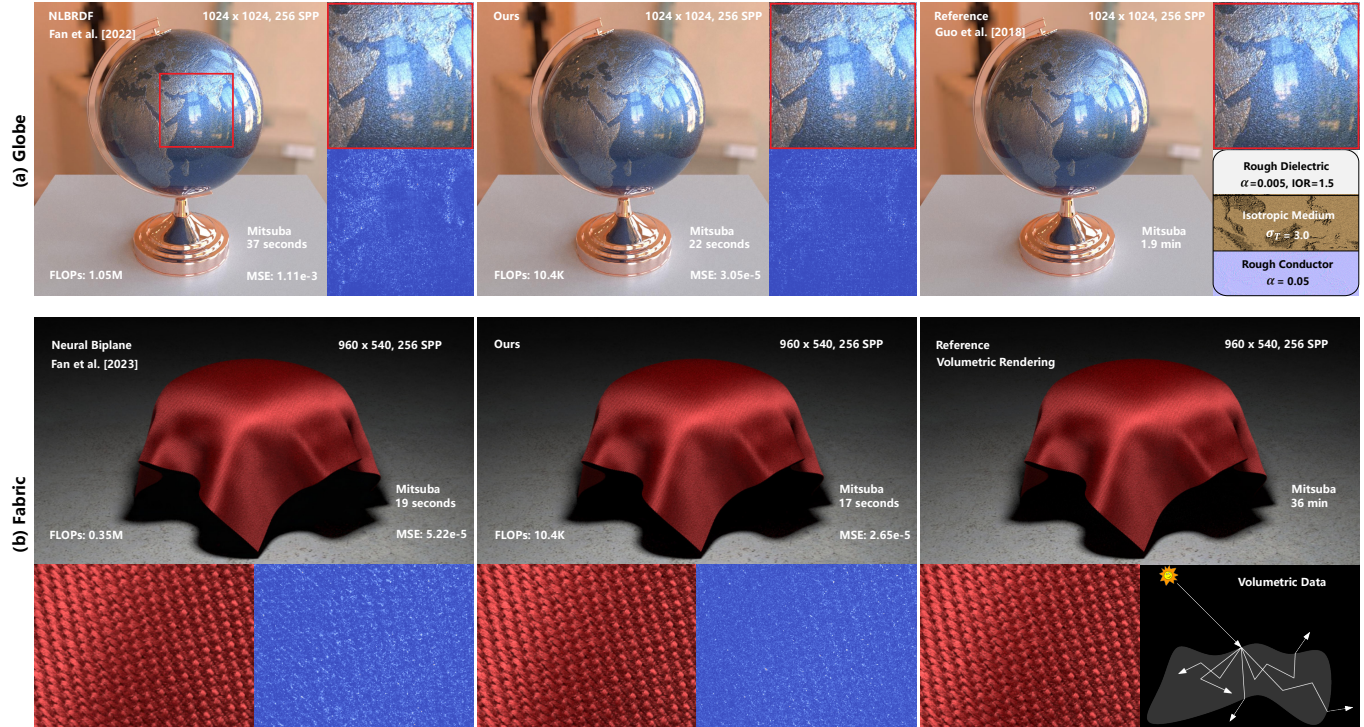


Fig. 8. **Accelerating physically based simulation.** We also demonstrate the comparison with the recent state-of-the-art neural approach, including NLBRDF [Fan et al. 2022] and Neural Biplane [Fan et al. 2023]. **(a) Simulation from Layered BRDF [Guo et al. 2018].** Our method requires quarter the time consumption compared to the simulation. **(b) Simulation from volume rendering.** The fabric is rendered from micro-CT volumetric data, using the microflake phase function. Our method requires almost one percent times compared to the simulation. Additionally, our method demonstrates superior results and performances compared with SOTA neural approaches in both scenes. We implement our methods in Mitsuba (an offline renderer) for fair comparison.

et al. 2023]. Furthermore, to demonstrate the application of accelerating physically-based simulation, we employ layered material simulator [Guo et al. 2018] and volume rendering using microflake phase function to generate realistic and complex appearances.

Table 3. **Average image-based losses** of representation methods from Figure 5 over all MERL materials.

Methods	MAE ↓	RMSE ↓	SSIM ↓
GGX [Walter et al. 2007]	0.0189	0.0206	0.969
Low et al. [2012]	0.0080	0.0088	0.986
Dupuy et al. [2015]	0.0174	0.0190	0.976
NPF [Bagher et al. 2016]	0.0056	0.0062	0.990
NBRDF [Sztrajman et al. 2021]	0.0028	0.0033	0.995
Ours	0.0017	0.0031	0.994

5.2 Quality Validation

It’s a standard practice to evaluate BRDF models or tune parameters of analytical models on measured reflectance data. The fitting results on MERL measurements are demonstrated in Figure 5. Our method achieves the most faithful rendering among both the diffuse, glossy, and specular materials. The quantitative results on the whole MERL measurement are shown in Table 3. We report the

mean absolute error (MAE), root mean squared error (RMSE), and structural similarity index measure (SSIM) on the rendered image, following NBRDF [Sztrajman et al. 2021].

Anisotropic BRDF. Our sphere data structure is designed to support both isotropic and anisotropic materials. This flexibility attribute to the factorized design and grid pruning. In figure 6, we demonstrate the representation quality of anisotropic materials from the RGL database. NBRDF [Sztrajman et al. 2021] struggles in representing high-frequency changes in some anisotropic BRDFs (such as MORPHO-MELENAUS) due to the low frequency spectral bias [Rahaman et al. 2019] of the pure-MLP in NBRDF. In contrast, benefits from the well-characterized *bidirection encoding*, our methods can reproduce the high-frequency reflectance distribution effective.

Sparse Measurement. Rendering a sparse measured BRDF directly may encounter visual artifact, and a time-consuming nearest neighbor search is necessary for rendering smooth results, for which the sparse measurements are solely used for rendering but are often used for validating analytical reflectance models. In order to evaluate the scalability to sparse measurement of NeuBRDF, we employ sparse BRDFs database of special coating [Ferrero et al. 2014] (hundreds of samples) and sparse SVBRDF of UBO2019 [Merzbach et al. 2019] (100 samples per pixel). The rendering results are shown in

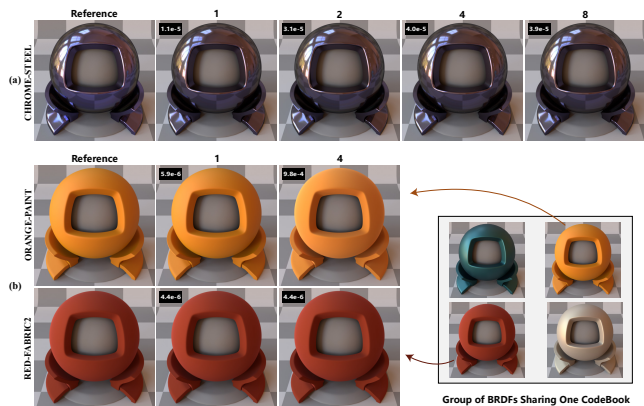


Fig. 9. **Sharing codebook across multiple instances.** The digits above images represent the number of instances sharing one codebook. We show the MSE in top-left corner. (a) Representation quality degenerates as the size of belonging material group increases. (b) We demonstrate the ability of neural primitives generalizing to different colors.

Figure 7. The smooth surface reflectance benefits from the inherent hierarchy of HEALPix, which enables the adaptive grid pruning for arbitrary sparse measurement.

Sharing Codebook. The neural reflectance primitives stored in a standalone codebook are independent of the per-instance sphere feature-grid, which offers the opportunity for maximizing the memory-quality by sharing codebook between material instances. We illustrate the representation quality in Figure 9. (a) shows the degeneration of rendering quality as the number of instances sharing one codebook increase; (b) shows the comparison of a cluster of materials represented with and without shared codebook. Figure 11 (top right) illustrates the overall degeneration of MERL when sharing codebook, evaluated on the raw reflectance data.

5.3 Extension Applications

Accelerating Physically Based Simulation. Reflectance models designed for photorealistic rendering are often layered [Guillén et al. 2020; Guo et al. 2018; Jakob et al. 2014]. By constructing various interface layers and internal media, these physical methods can cover a wide range of appearances. Evaluating such models is usually achieved through light transport between layers, simulated by Monte Carlo. Since our method is agnostic of the internal light-layer interactions it can be directly used for accelerating these physical-based methods for various layered configurations.

In many complex scenes, these layered BRDF methods often use albedo texture, normal map, or spatially varying scattering/absorption coefficient in internal layers. As a compatible solution, we still use the plug-and-play neural texture \mathcal{T} . The neural texture can be considered as a blend of multiple internal textures. With the expense of building the reflectance data (hours) and training (< 1 hour), our method can drastically reduce the cost at rendering; see Figure 8 for an illustration. Our approach performs surprisingly well in such a complicated scene. We use the default base framework together with a $800 \times 400 \times 8$ neural texture to capture the spatially varying effects. These results demonstrate that our approach generalizes



Fig. 10. **BTF compression on UBO2014.** Each data contains $400 \times 400 \times 22801$ RGB measurements, which occupancy ~ 500 MB storage (compressed). Simply with a $128 \times 128 \times 4$ neural texture (~ 131 KB), NeuBRDF (~ 95 KB) can capture these spatially varying effects, resulting in a compression ratio of thousands of times. (Storage of NeuBRDF and neural texture are computed in *fp16*.)

well to complex designs and can produce highly realistic results in a much smaller computation resource compared with either the physical simulations or the recent neural-based approaches.

BTF Compression. Tabulating an isotropic BRDF consumes tens of megabytes memory and becomes prohibitive for spatially varying material, impeding the network transfer and runtime loading. Our framework can be easily extended for the compression purpose, the BTF compression results are illustrated in Figure 10. The convincing results of NeuBRDF with a naive neural texture plugin suggest the feasibility of decoupling spatially varying effect and bidirectional $\omega_{i,o}$, which is also proven in neural biplane [Fan et al. 2023].

Similarly, neural texture compression (NTC) [Vaidyanathan et al. 2023] is proposed to compress the texture. However, they only operate on the image space and rely on an extra reflectance model to consume the decoded image textures. Instead, we consider the reflectance model per se. We note that a highly specific neural texture like the neural mipmap texture in NTC is also compatible with our framework.

5.4 Ablation Studies

Model Configuration. We investigate the impact of MLP channels, feature-grid resolution (N_{side}), codebook bitwidth, and codebook feature dimension; shown in Figure 11 (left two columns). In order to fully validate the model at different configurations, we report the MSE on the raw reflectance data rather than the rendered image that not yields full coverage of the bidirection space.

Codebook and Low-bit Quantization. The primitive indexing is exactly the same with vector quantization in the perspective of quantization. To this end, we conduct ablation study on (1) the model without codebook, where the sphere grid allocates bulky

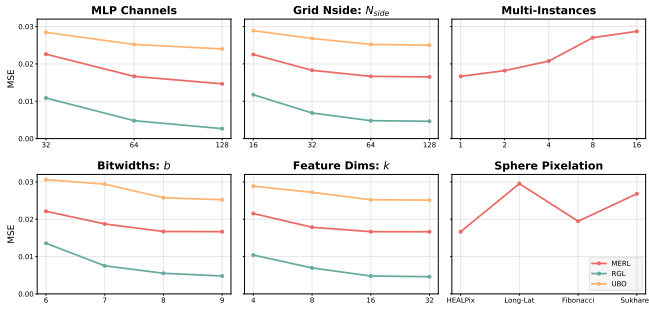


Fig. 11. **Ablation studies on different model configurations.** MSE is computed on the raw data rather than the rendered image. Multiple material instances are selected from a same cluster. Sphere pixelations have similar number of grid points for fair comparison.

features instead of lightweight integer indices, (2) and the model with low-bit quantization. The MSE results on MERL raw data and the required parameters are shown in Table 4. In addition to the memory efficiency, the use of codebook can alleviate the overfitting drawback of feature-grid and allow the sharing of the primitives across instances as described in previous section. We implement low-bit quantization by simulating quantization along the line of neural image compression [Ballé et al. 2016; Vaidyanathan et al. 2023].

Table 4. **Comparison in the view of quantization.** The codebook is also a quantization technique, for which we compare it with low-bit (4b) quantization. Experimental results show that it consumes less memory and performs better than low-bit quantization in this case. Memory costs are computed in *fp16* except the low-bit quantization, and the MLP is not taken into account.

	MSE ↓	Memory Cost ↓	Ratio ↓
w/o Quantization	0.0160	1.60MB	1
w Low-bit	0.0189	0.40MB	0.25
w CodeBook (ours)	0.0167	0.07MB	0.045

Sphere Pixelation. The design of sphere pixelation is critical to the success of our method. We demonstrate representing quality in Figure 11 (bottom right), where the grid resolutions (or the number of grid points) are managed as close as possible for each pixelation. Both of the other pixelations are manually tailored for BRDF representation, which are similar with that of HEALPix described in Section 3.2.2. Regardless of the exclusive merit of *hierarchy* of HEALPix, the model with HEALPix achieves best representation results. Although the Fibonacci pixelation is comparable in terms of MSE, the indexing time of Fibonacci is about *5ms* in contrast to the *0.5ms* of HEALPix. We expect the HEALPix with our tailored and delicate adaptation for BRDFs can be the basic data structure in material representation, like the Octree in geometry representation.

Runtime Time Breakdown. We implement our NeuBRDF in Falcor for real-time testing. Please refer to Figure 1 for the time breakdown of our method. Evaluating our reflectance models takes about *4.5ms* in a 5 – *maxdepth* path tracer at full resolution (1 SPP, 1920×1080),

which is agnostic to the material type. The bulk of the time is taken by fully connected layers. Currently, the fully connected layer is simply implemented in shader without any bells and whistles.

6 CONCLUSIONS

In this article, we propose a neural reflectance model that is potentially a choice for achieving realistic appearance in real-time rendering applications. The proposed method is also a unified framework that can represent a variety of materials, which can be used for measured data compression, fitting sparse measurements, physical-based methods acceleration and so on. The key components to the effectiveness consists of the delicately designed sphere data structure and neural reflectance primitives. In the future, we will exploit more material application based on such architecture, *i.e.* spherically distributed primitives with a tiny-MLP decoder, such as material editing and material acquisition in inverse rendering.

REFERENCES

- Mahdi M Bagher, John Snyder, and Derek Nowrouzezahrai. 2016. A non-parametric factor microfacet model for isotropic BRDFs. *ACM Transactions on Graphics (TOG)* 35, 5 (2016), 1–16.
- Johannes Ballé, Valero Laparra, and Eero P Simoncelli. 2016. End-to-end optimized image compression. *arXiv preprint arXiv:1611.01704* (2016).
- Yoshua Bengio, Nicholas Léonard, and Aaron C. Courville. 2013. Estimating or Propagating Gradients Through Stochastic Neurons for Conditional Computation. *CoRR abs/1308.3432* (2013).
- Brent Burley and Walt Disney Animation Studios. 2012. Physically-based shading at disney. In *ACM SIGGRAPH*, Vol. 2012. vol. 2012, 1–7.
- Kristin J Dana, Bram Van Ginneken, Shree K Nayar, and Jan J Koenderink. 1999. Reflectance and texture of real-world surfaces. *ACM Transactions On Graphics (TOG)* 18, 1 (1999), 1–34.
- Jonathan Dupuy, Eric Heitz, Jean-Claude Iehl, Pierre Poulin, and Victor Ostromoukhov. 2015. Extracting microfacet-based brdf parameters from arbitrary materials with power iterations. In *Computer Graphics Forum*, Vol. 34. Wiley Online Library, 21–30.
- Jonathan Dupuy and Wenzel Jakob. 2018. An adaptive parameterization for efficient material acquisition and rendering. *ACM Transactions on graphics (TOG)* 37, 6 (2018), 1–14.
- Jiahui Fan, Beibei Wang, Milos Hasan, Jian Yang, and Ling-Qi Yan. 2022. Neural Layered BRDFs. In *ACM SIGGRAPH 2022 Conference Proceedings*. 1–8.
- Jiahui Fan, Beibei Wang, Milos Hasan, Jian Yang, and Ling-Qi Yan. 2023. Neural Biplane Representation for BTF Rendering and Acquisition. In *ACM SIGGRAPH 2023 Conference Proceedings*. 1–11.
- Alejandro Ferrero, Esther Perales, Ana M Rabal, J Campos, Francisco Miguel Martínez-Verdú, Elizabet Chorro, and A Pons. 2014. Color representation and interpretation of special effect coatings. *JOSA A* 31, 2 (2014), 436–447.
- Sara Fridovich-Keil, Alex Yu, Matthew Tancik, Qinhong Chen, Benjamin Recht, and Angjoo Kanazawa. 2022. Plenoxels: Radiance Fields Without Neural Networks. In *Proceedings of the IEEE/CVF Conference on Computer Vision and Pattern Recognition*. 5501–5510.
- Álvaro González. 2010. Measurement of areas on a sphere using Fibonacci and latitude–longitude lattices. *Mathematical Geosciences* 42, 1 (2010), 49–64.
- Krzysztof M Gorski, Eric Hivon, Anthony J Banday, Benjamin D Wandelt, Frode K Hansen, Mstvos Reinecke, and Matthia Bartelmann. 2005. HEALPix: A framework for high-resolution discretization and fast analysis of data distributed on the sphere. *The Astrophysical Journal* 622, 2 (2005), 759.
- Ibón Guillén, Julio Marco, Diego Gutierrez, Wenzel Jakob, and Adrian Jarabo. 2020. A general framework for pearlescent materials. *ACM Transactions on Graphics (TOG)* 39, 6 (2020), 1–15.
- Yu Guo, Miloš Hašan, and Shuang Zhao. 2018. Position-free Monte Carlo simulation for arbitrary layered BSDFs. *ACM Transactions on Graphics (ToG)* 37, 6 (2018), 1–14.
- Bingyang Hu, Jie Guo, Yanjun Chen, Mengtian Li, and Yanwen Guo. 2020. DeepBRDF: A deep representation for manipulating measured BRDF. In *Computer Graphics Forum*, Vol. 39. Wiley Online Library, 157–166.
- Wenzel Jakob. 2010. Mitsuba renderer. <https://mitsuba-renderer.org>.
- Wenzel Jakob, Eugene D’Eon, Otto Jakob, and Steve Marschner. 2014. A comprehensive framework for rendering layered materials. *ACM Transactions on Graphics* 33, 4 (2014), 1–14.
- Simon Kallweit, Petrik Clarberg, Craig Kolb, Tom’as Davidovič, Kai-Hwa Yao, Theresa Foley, Yong He, Lifan Wu, Lucy Chen, Tomas Akenine-Möller, Chris Wyman, Cyril

- Crassin, and Nir Benty. 2022. The Falcor Rendering Framework. <https://github.com/NVIDIAGameWorks/Falcor> <https://github.com/NVIDIAGameWorks/Falcor>.
- Diederik P Kingma and Jimmy Ba. 2014. Adam: A method for stochastic optimization. *arXiv preprint arXiv:1412.6980* (2014).
- Jan J Koenderink, Andrea J Van Doorn, and Marigo Stavridi. 1996. Bidirectional reflection distribution function expressed in terms of surface scattering modes. In *Computer Vision—ECCV’96: 4th European Conference on Computer Vision Cambridge, UK, April 15–18, 1996 Proceedings Volume II 4*. Springer, 28–39.
- Alexandr Kuznetsov. 2021. NeuMIP: Multi-resolution neural materials. *ACM Transactions on Graphics (TOG)* 40, 4 (2021).
- Lutz Latta and Andreas Kolb. 2002. Homomorphic factorization of BRDF-based lighting computation. *ACM Transactions on Graphics (TOG)* 21, 3 (2002), 509–516.
- Lingjie Liu, Jiatao Gu, Kyaw Zaw Lin, Tat-Seng Chua, and Christian Theobalt. 2020. Neural sparse voxel fields. *Advances in Neural Information Processing Systems* 33 (2020), 15651–15663.
- Joakim Löw, Joel Kronander, Anders Ynnerman, and Jonas Unger. 2012. BRDF models for accurate and efficient rendering of glossy surfaces. *ACM Transactions on Graphics (TOG)* 31, 1 (2012), 1–14.
- Wojciech Matusik, Hanspeter Pfister, Matt Brand, and Leonard McMillan. 2003. A Data-Driven Reflectance Model. *ACM Transactions on Graphics* 22, 3 (July 2003), 759–769.
- Michael D McCool, Jason Ang, and Anis Ahmad. 2001. Homomorphic factorization of BRDFs for high-performance rendering. In *Proceedings of the 28th annual conference on Computer graphics and interactive techniques*. 171–178.
- Sebastian Merzbach, Max Hermann, Martin Rump, and Reinhard Klein. 2019. Learned Fitting of Spatially Varying BRDFs. *Computer Graphics Forum* 38, 4 (July 2019). <https://cg.cs.uni-bonn.de/svbrdfs/>
- Ben Mildenhall, Pratul P Srinivasan, Matthew Tancik, Jonathan T Barron, Ravi Ramamoorthi, and Ren Ng. 2021. Nerf: Representing scenes as neural radiance fields for view synthesis. *Commun. ACM* 65, 1 (2021), 99–106.
- Thomas Müller, Alex Evans, Christoph Schied, and Alexander Keller. 2022. Instant neural graphics primitives with a multiresolution hash encoding. *arXiv preprint arXiv:2201.05989* (2022).
- Jeong Joon Park, Peter Florence, Julian Straub, Richard Newcombe, and Steven Lovegrove. 2019. Deepsdf: Learning continuous signed distance functions for shape representation. In *Proceedings of the IEEE/CVF conference on computer vision and pattern recognition*. 165–174.
- Adam Paszke, Sam Gross, Francisco Massa, Adam Lerer, James Bradbury, Gregory Chanan, Trevor Killeen, Zeming Lin, Natalia Gimelshein, Luca Antiga, et al. 2019. Pytorch: An imperative style, high-performance deep learning library. *Advances in neural information processing systems* 32 (2019).
- Songyou Peng, Michael Niemeyer, Lars Mescheder, Marc Pollefeys, and Andreas Geiger. 2020. Convolutional occupancy networks. In *European Conference on Computer Vision*. Springer, 523–540.
- Nathanaël Perraudin, Michaël Defferrard, Tomasz Kacprzak, and Raphael Sgier. 2019. DeepSphere: Efficient spherical convolutional neural network with HEALPix sampling for cosmological applications. *Astronomy and Computing* 27 (2019), 130–146.
- Nasim Rahaman, Aristide Baratin, Devansh Arpit, Felix Draxler, Min Lin, Fred Hamprecht, Yoshua Bengio, and Aaron Courville. 2019. On the spectral bias of neural networks. In *International Conference on Machine Learning*. PMLR, 5301–5310.
- Gilles Rainer, Abhijeet Ghosh, Wenzel Jakob, and Tim Weyrich. 2020. Unified neural encoding of BTfs. In *Computer Graphics Forum*, Vol. 39. Wiley Online Library, 167–178.
- Gilles Rainer, Wenzel Jakob, Abhijeet Ghosh, and Tim Weyrich. 2019. Neural btf compression and interpolation. In *Computer Graphics Forum*, Vol. 38. Wiley Online Library, 235–244.
- Aleksandr G Sukharev. 1971. Optimal strategies of the search for an extremum. *U. S. S. R. Comput. Math. and Math. Phys.* 11, 4 (1971), 119–137.
- Alejandro Sztrajman, Gilles Rainer, Tobias Ritschel, and Tim Weyrich. 2021. Neural BRDF Representation and Importance Sampling. In *Computer Graphics Forum*, Vol. 40. Wiley Online Library, 332–346.
- Towaki Takikawa, Alex Evans, Jonathan Tremblay, Thomas Müller, Morgan McGuire, Alec Jacobson, and Sanja Fidler. 2022. Variable bitrate neural fields. In *ACM SIG-GRAPH 2022 Conference Proceedings*. 1–9.
- Towaki Takikawa, Joey Litalien, Kangxue Yin, Karsten Kreis, Charles Loop, Derek Nowrouzezahrai, Alec Jacobson, Morgan McGuire, and Sanja Fidler. 2021. Neural geometric level of detail: Real-time rendering with implicit 3D shapes. In *Proceedings of the IEEE/CVF Conference on Computer Vision and Pattern Recognition*. 11358–11367.
- Justus Thies, Michael Zollhöfer, and Matthias Nießner. 2019. Deferred neural rendering: Image synthesis using neural textures. *ACM Transactions on Graphics (TOG)* 38, 4 (2019), 1–12.
- Karthik Vaidyanathan, Marco Salvi, Bartłomiej Wronski, Tomas Akenine-Möller, Pontus Ebelin, and Aaron Lefohn. 2023. Random-Access Neural Compression of Material Textures. *arXiv preprint arXiv:2305.17105* (2023).
- Bruce Walter, Stephen R Marschner, Hongsong Li, and Kenneth E Torrance. 2007. Microfacet models for refraction through rough surfaces. In *Proceedings of the 18th Eurographics conference on Rendering Techniques*. 195–206.
- Stephen H Westin, James R Arvo, and Kenneth E Torrance. 1992. Predicting reflectance functions from complex surfaces. In *Proceedings of the 19th annual conference on Computer graphics and interactive techniques*. 255–264.
- Chuankun Zheng, Ruzhang Zheng, Rui Wang, Shuang Zhao, and Hujun Bao. 2021. A Compact Representation of Measured BRDFs Using Neural Processes. *ACM Transactions on Graphics (TOG)* 41, 2 (2021), 1–15.